

COARSE-FINE SPECTRAL-AWARE DEFORMABLE CONVOLUTION FOR HYPERSPECTRAL IMAGE RECONSTRUCTION

Jincheng Yang¹, Lishun Wang², Miao Cao², Huan Wang², Yinping Zhao¹, Xin Yuan²

¹Northwestern Polytechnical University, Xi'an, China

²Westlake University, Hangzhou, China

ABSTRACT

We study the inverse problem of Coded Aperture Snapshot Spectral Imaging (CASSI), which captures a spatial-spectral data cube using snapshot 2D measurements and uses algorithms to reconstruct 3D hyperspectral images (HSI). However, current methods based on Convolutional Neural Networks (CNNs) struggle to capture long-range dependencies and non-local similarities. The recently popular Transformer-based methods are poorly deployed on downstream tasks due to the high computational cost caused by self-attention. In this paper, we propose Coarse-Fine Spectral-Aware Deformable Convolution Network (CFSDCN), applying deformable convolutional networks (DCN) to this task for the first time. Considering the sparsity of HSI, we design a deformable convolution module that exploits its deformability to capture long-range dependencies and non-local similarities. In addition, we propose a new spectral information interaction module that considers both coarse-grained and fine-grained spectral similarities. Extensive experiments demonstrate that our CFSDCN significantly outperforms previous state-of-the-art (SOTA) methods on both simulated and real HSI datasets.

Index Terms— Compressive sensing, coded aperture snapshot spectral imaging (CASSI), hyperspectral image reconstruction, deformable convolution, spectral similarities

1. INTRODUCTION

Hyperspectral images (HSI) can capture data over a larger number of spectral bands than traditional three-color (RGB) images, thereby storing more comprehensive spectral information. This spectral characteristic enables HSIs to be extensively employed in fields such as image recognition [1], object detection [2], remote sensing [3], *etc.*

Coded Aperture Snapshot Spectral Imaging (CASSI) captures HSI by using coded apertures and dispersors across different wavelengths to modulate the HSI signal and combine them into two-dimensional compressed measurements, greatly improving frame rates. But it also brings with it the complex task of accurately recovering HSI from compressed measurements.

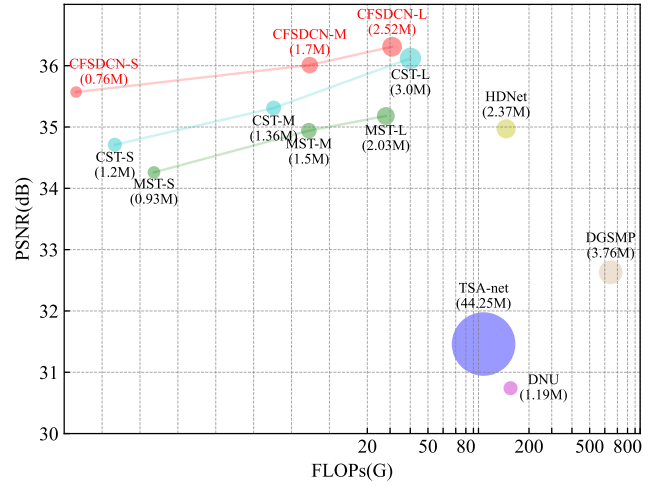


Fig. 1: Comparison of PSNR-Params-FLOPs with some previous SOTA methods. The vertical axis represents PSNR, and the horizontal axis represents FLOPs. The size of the scatter points is related to the parameters of the model.

In recent years, there have been four main solutions to this task. (i) Traditional methods mainly rely on model-based techniques that utilize hand-crafted image priors [4, 5]. They are rooted in strong theoretical foundations and provide interpretability, but their reliance on manual parameter tuning hinders efficiency and better performance. (ii) Plug-and-play (PnP) algorithms [6, 7] stand out by seamlessly integrating pre-trained denoising networks within traditional model-based paradigms. However, their reliance on static, immutable networks limits their potential. (iii) The end-to-end (E2E) [8, 9, 10, 11] strategy mainly utilizes convolutional neural networks (CNN) to provide a direct route from measurement to HSI. But they often ignore the nuances of specific imaging systems. (iv) Traditional deep unrolling methods [12, 13, 14] combine iterative optimization with deep neural networks to combine the power of deep learning with the transparency of traditional methods. But they have difficulty solving system-specific degradation problems and HSI long-range dependencies.

With the remarkable success of transformers [15] in lan-

guage models, Vision Transformers (ViTs) [16] have swept through the field of computer vision. They have also achieved outstanding results in HSI reconstruction [17, 18]. The Multi-head Self-Attention (MSA) module of the Transformer excels in capturing non-local similarities and long-range dependencies, addressing the limitations of CNN-based reconstruction methods. However, the computational requirements of global attention lead to a significant computational load and high memory complexity. Therefore, it faces challenges in being applied to downstream tasks.

To address the aforementioned issues, in this paper, we propose a novel approach, CFSDCN, for HSI reconstruction. The contributions of our work can be summarized as follows:

- i) We propose a new CNN-based end-to-end method, CFSDCN, for HSI reconstruction. Use deformable convolutions to capture long-range dependencies and non-local similarities of spatially sparse HSI. To the best of my knowledge, this is the first attempt to apply deformable convolution to this task.
- ii) We propose a novel Spectral Information Perception module composed of convolutions, named CFSAB (Coarse-Fine Spectral-Aware Block). This module, through the use of large kernel and point-wise convolutions, simultaneously captures both coarse-grained and fine-grained spectral similarities.
- iii) Our model achieves SOTA performance at extremely low computational cost and parameter size in all simulation scenarios of the same scale. Furthermore, our CFSDCN achieves more pleasing results on real datasets.

2. MATHEMATICAL MODEL OF CASSI

The schematic of the CASSI system is briefly illustrated in Fig. 2. The degradation of the CASSI system can be attributed to various factors, including physical masks, dispersive prisms, and 2D imaging sensors. We assume the input 3D HSI data cube to be $\mathbf{F} \in \mathbb{R}^{H \times W \times N_\lambda}$, where H , W , and N_λ respectively represent the height, width, and number of wavelengths of the HSI. The physical mask $\mathbf{M}^* \in \mathbb{R}^{H \times W}$ serves as the modulator for the HSI signal, representing the modulated image across wavelengths

$$\mathbf{F}'_{n_\lambda} = \mathbf{F}_{n_\lambda} \odot \mathbf{M}^*, \quad (1)$$

where \mathbf{F}' represents the modulated, $n_\lambda \in [1, \dots, N_\lambda]$ denotes the n_λ^{th} wavelength of the modulated image, \odot represents the element-wise product. Therefore, after modulation, the HSI \mathbf{F}' undergoes a displacement during the dispersion process through the disperser, expressed as

$$\mathbf{F}''_{n_\lambda}(u, v, n_\lambda) = \mathbf{F}'_{n_\lambda}(u, v + d_{n_\lambda}, n_\lambda), \quad (2)$$

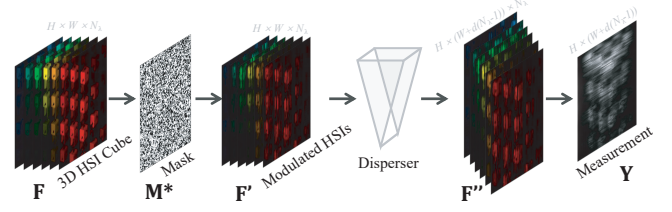


Fig. 2: A schematic diagram of CASSI.

where $\mathbf{F}'' \in \mathbb{R}^{H \times (W + d_{N_\lambda}) \times N_\lambda}$, (u, v) represents the coordinate system on the detector plane, d_{n_λ} represents the shifted distance of the n_λ^{th} wavelength. Finally, the 2D compress measurements $\mathbf{Y} \in \mathbb{R}^{H \times (W + d(N_\lambda - 1))}$ captured by CASSI can be represented as

$$\mathbf{Y} = \sum_{n_\lambda=1}^{N_\lambda} \mathbf{F}''_{n_\lambda} + \mathbf{G}, \quad (3)$$

where $\mathbf{G} \in \mathbb{R}^{H \times (W + d(N_\lambda - 1))}$ is the imaging noise on the measurement introduced during the system imaging process. Our task is to restore this 2D measurement \mathbf{Y} captured by CASSI into the 3D spatial-spectral data cube \mathbf{F} we desired.

3. METHOD

3.1. Overall Architecture

The overall structure of CFSDCN is shown in the Fig. 3 (a). For a given 2D measurement $\mathbf{Y} \in \mathbb{R}^{H \times (W + d(N_\lambda - 1))}$, we reverse the dispersion process (Eq. (2)) and shift back the measurement to obtain the input signal $\mathbf{H} \in \mathbb{R}^{H \times W \times N_\lambda}$ as

$$\mathbf{H}(x, y, n_\lambda) = \mathbf{Y}(x, y - d(\lambda_n - \lambda_c)). \quad (4)$$

Subsequently, we concatenate \mathbf{H} with the 3D mask $\mathbf{M} \in \mathbb{R}^{H \times W \times N_\lambda}$ and employ a *conv* 1×1 (a convolution operation with a kernel size of 1) to obtain the initialized feature $\mathbf{X} \in \mathbb{R}^{H \times W \times N_\lambda}$. Then, referring to the Unet structure, the main architecture of our network consists of three parts: encoder, bottleneck, and decoder. Each layer of encoder consists of N_1 Coarse-Fine Spectral-Aware Deformable Convolution Blocks (CFSDCBs) and downsampling, while each layer of decoder consists of N_2 CFSDCBs and corresponding upsampling. The bottleneck contains N_3 CFSDCBs. The structure of CFSDCB is shown in Fig. 3 (a). Finally, a *conv* 3×3 is used to change the output of decoder $\mathbf{X}_d \in \mathbb{R}^{H \times W \times C}$ to the residual HSIs $\mathbf{R} \in \mathbb{R}^{H \times W \times N_\lambda}$. And the reconstructed HSIs \mathbf{X}' can be obtained by the sum of \mathbf{X} and \mathbf{R} , i.e., $\mathbf{X}' = \mathbf{X} + \mathbf{R}$.

3.2. Spatial-aware Deformable Convolution Module

Grouped Deformable Convolution. In traditional Convolutional Neural Network (CNN) based approaches, effectively leveraging the inherent non-local similarity in hyperspectral images (HSI) poses a challenge. To solve this problem, we introduce deformable convolution, which captures non-local

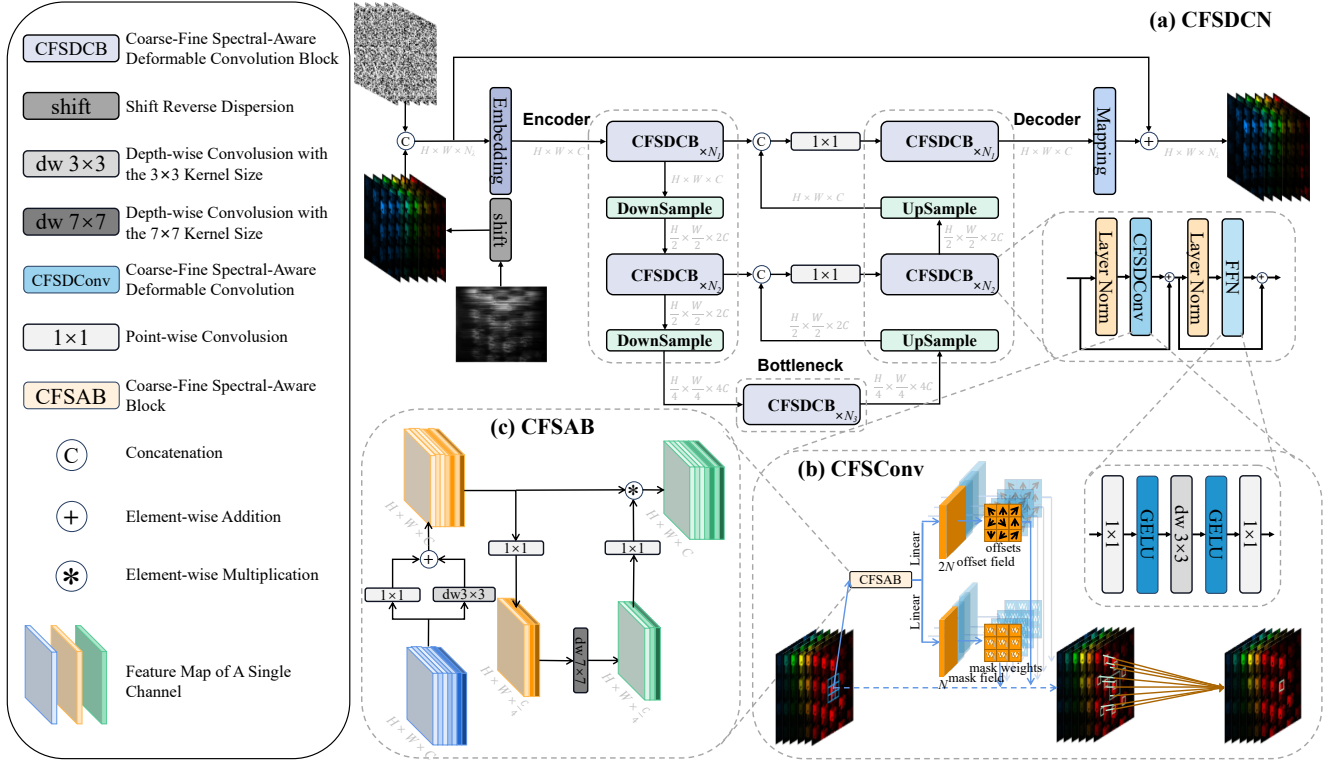


Fig. 3: Details of CFSDCN. (a) Overall structure diagram of CFSDCN. (b) Schematic diagram of Coarse-Fine Spectral-Aware Deformable Convolution (CFSCConv). (c) Schematic diagram of Coarse-Fine Spectral-Aware Block (CFSAB).

features and long-range dependencies well through an offset. Moreover, the 3×3 size convolution kernel is friendly in terms of speed and calculation amount, so our goal is to explore the potential of deformable convolution in HSI reconstruction. We introduce Grouped Deformable Convolution [19] to extract spatially different feature information of the spectrum. Fig. 3 (b) showcases the structure of our deformable convolution used in our approach. For each pixel point p_0 of the input $\mathbf{X}_{\text{in}} \in \mathbb{R}^{H \times W \times C}$, the fundamental principle of our deformable convolution can be expressed as

$$X(p_0) = \sum_{g=1}^G \sum_{k=1}^K w_g m_{gk} x_g(p_0 + p_k + \Delta p_{gk}), \quad (5)$$

where G represents the total number of aggregation groups similar to the multi-head concept, K indicates the total number of subsample points under the changed kernel size, and w_g refers to the location-irrelevant projection weights of each group, m_{gk} denotes the modulation scalar for the k -th sampling point in the g -th group, x_g is the input feature mapping of the slice, and Δp_{gk} is the offset of the k -th sampling point in the g -th group relative to the original p_k sampling point.

3.3. Coarse-Fine Spectral-Aware Module

In the proposal and application of deformable convolutions, the similarity and attention across channels have not been ad-

equately emphasized and utilized, which is a crucial property for HSIs. Therefore, we explore CNN-based spectral perception methods to effectively utilize this aspect of HSIs.

Fine-grained spectral similarity. We note that in DCN, to reduce the number of parameters, they employ depth-wise separable convolutions instead of conventional convolution operations. This approach does not allow the weights of offsets and masks to consider the spectral similarity at the same location across different spectra brought about by the eventual point-wise convolution, which we refer to as fine-grained spectral similarity. Therefore, as shown in the left part of Fig. 3 (c), we add a parallel branch to learn this fine-grained spectral similarity

$$\mathbf{X}_p = \text{Conv}_{1 \times 1}(\mathbf{X}_{\text{inp}}), \quad (6)$$

$$\mathbf{X}_{\text{fine}} = \text{DWConv}_{3 \times 3}(\mathbf{X}_{\text{inp}}) + \mathbf{X}_{\text{sconv}}, \quad (7)$$

where $\mathbf{X}_{\text{inp}} \in \mathbb{R}^{H \times W \times C}$ represents the input of the CFSConv, $\mathbf{X}_p \in \mathbb{R}^{H \times W \times C}$ denotes the added parallel branch for capturing fine-grained spectral similarities, $\mathbf{X}_{\text{fine}} \in \mathbb{R}^{H \times W \times C}$ denotes the result of fine-gained spectral aware. We employ a point-wise convolution to facilitate interaction between information at the same spatial positions but across different spectral bands, and then integrate this output back into the original branch. This integration enables the model to acquire fine-grained spectral information.

Table 1: Comparisons of Params, FLOPs, PSNR (upper entry in each cell), and SSIM (lower entry in each cell) of different methods on 10 simulation scenes (Scene1-Scene10). Best results are in bold and the second-best results are underlined.

Algorithms	Params	GFLOPs	Scene1	Scene2	Scene3	Scene4	Scene5	Scene6	Scene7	Scene8	Scene9	Scene10	Average
TwIST [4]	-	-	25.16 0.700	23.02 0.604	21.40 0.711	30.19 0.851	21.41 0.635	20.95 0.644	22.20 0.643	21.82 0.650	22.42 0.690	22.67 0.569	23.12 0.669
GAP-TV [5]	-	-	26.82 0.754	22.89 0.610	26.31 0.802	30.65 0.852	23.64 0.703	21.85 0.663	23.76 0.688	21.98 0.655	22.63 0.682	23.10 0.584	24.36 0.669
DeSCI [20]	-	-	27.13 0.748	23.04 0.620	26.62 0.818	34.96 0.897	23.94 0.706	22.38 0.683	24.45 0.743	22.03 0.673	24.56 0.732	23.59 0.587	25.27 0.721
λ -net [21]	62.64M	117.98	30.10 0.849	28.49 0.805	27.73 0.870	37.01 0.934	26.19 0.817	28.64 0.853	26.47 0.806	26.09 0.831	27.50 0.826	27.13 0.816	28.53 0.841
HSSP [22]	-	-	31.48 0.858	31.09 0.842	28.96 0.823	34.56 0.902	28.53 0.808	30.83 0.877	28.71 0.824	30.09 0.881	30.43 0.868	28.78 0.842	30.35 0.852
DNU [12]	1.19M	163.48	31.72 0.863	31.13 0.846	29.99 0.845	35.34 0.908	29.03 0.833	30.87 0.887	28.99 0.839	30.13 0.885	31.03 0.876	29.14 0.849	30.74 0.863
DIP-HSI [6]	33.85M	64.42	32.68 0.890	27.26 0.833	31.30 0.914	40.54 0.962	29.79 0.900	30.39 0.877	28.18 0.913	29.44 0.874	34.51 0.927	28.51 0.851	31.26 0.894
TSA-net [8]	44.25M	110.06	32.03 0.892	31.00 0.858	32.25 0.915	39.19 0.953	29.39 0.884	31.44 0.908	30.32 0.878	29.35 0.888	30.01 0.890	29.59 0.874	31.46 0.894
DGSMP [13]	3.76M	646.65	33.26 0.915	32.09 0.898	33.06 0.925	40.54 0.964	28.86 0.882	33.08 0.937	30.74 0.886	31.55 0.923	31.66 0.911	31.44 0.925	32.63 0.917
HDNet [9]	2.37M	154.76	35.14 0.935	35.67 0.940	36.03 0.943	42.30 0.969	32.69 0.946	34.46 0.952	33.67 0.926	32.48 0.941	34.89 0.942	32.38 0.937	34.97 0.943
MST-S [17]	0.93M	12.96	34.71 0.930	34.45 0.925	35.32 0.943	41.50 0.967	31.90 0.933	33.85 0.943	32.69 0.911	31.69 0.933	34.67 0.939	31.82 0.926	34.26 0.935
MST-M [17]	1.50M	18.07	35.15 0.937	35.19 0.935	36.26 0.950	42.48 0.973	32.49 0.943	34.28 0.948	33.29 0.921	32.40 0.943	35.35 0.942	32.53 0.935	34.94 0.943
MST-L [17]	2.03M	28.15	35.40 0.941	35.87 0.944	36.51 0.953	42.27 0.973	32.77 0.947	34.80 0.955	33.66 0.925	32.67 0.948	35.39 0.949	32.50 0.941	35.18 0.948
CST-S [23]	1.20M	11.67	34.78 0.930	34.81 0.931	35.42 0.944	41.84 0.967	32.29 0.939	34.49 0.949	33.47 0.922	32.89 0.945	34.96 0.944	32.14 0.932	34.71 0.940
CST-M [23]	1.36M	16.91	35.16 0.938	35.60 0.942	36.57 0.953	42.29 0.972	32.82 0.948	35.15 0.956	33.85 0.927	33.52 0.952	35.28 0.946	32.84 0.940	35.31 0.947
CST-L [23]	3.00M	40.10	35.96 <u>0.949</u>	<u>36.84</u> <u>0.955</u>	<u>38.16</u> 0.962	42.44 0.975	33.25 0.955	35.72 <u>0.963</u>	<u>34.86</u> <u>0.944</u>	34.34 <u>0.961</u>	36.51 0.957	33.09 0.945	<u>36.12</u> <u>0.957</u>
CFSDCN-S (Ours)	0.76M	9.45	35.45 0.944	35.88 0.944	37.00 0.958	42.94 0.978	32.99 0.950	35.17 0.959	34.12 0.936	33.17 0.954	36.52 0.959	32.49 0.944	35.57 0.953
CFSDCN-M (Ours)	1.7M	18.1	35.59 0.947	36.58 0.954	37.94 <u>0.963</u>	<u>43.33</u> <u>0.982</u>	<u>33.30</u> <u>0.956</u>	35.38 0.964	34.36 0.939	33.46 0.959	<u>37.17</u> <u>0.964</u>	<u>32.97</u> <u>0.948</u>	36.01 <u>0.958</u>
CFSDCN-L (Ours)	2.52M	31.0	<u>35.93</u> 0.950	37.06 0.958	38.58 0.970	43.80 0.983	33.38 0.957	<u>35.52</u> 0.966	34.88 0.946	<u>33.51</u> 0.962	37.50 0.965	32.92 0.950	36.31 0.961

Coarse-grained spectral similarity. For coarse-grained spectral similarity, that is, the similarity between different locations across different spectral channels, we design a Large-kernel-guided Coarse-grained Spectral-aware(LCS) module. As shown in the right part of Fig. 3 (c), we use large kernel convolutions to increase the receptive field, capturing information between different positions, and then place it within a spectral information interaction module composed of point-wise convolutions

$$\mathbf{X}_{\text{down}} = \text{Conv}_{1 \times 1}(\mathbf{X}_{\text{fine}}), \quad (8)$$

$$\mathbf{X}_{\text{lkconv}} = \text{DWConv}_{7 \times 7}(\mathbf{X}_{\text{down}}), \quad (9)$$

$$\mathbf{X}_{\text{weight}} = \text{Conv}_{1 \times 1}(\mathbf{X}_{\text{Coarse}}), \quad (10)$$

where $\mathbf{X}_{\text{down}} \in \mathbb{R}^{H \times W \times C/4}$ refers to the result of X_{fine} after dimensionality reduction through point-wise convolution, representing the process of channel information fusion; $\mathbf{X}_{\text{lkconv}} \in \mathbb{R}^{H \times W \times C/4}$ indicates the coarse-grained information matrix obtained by gathering information around each pixel point via a depth-wise convolution with a large ker-

nel; $\mathbf{X}_{\text{weight}} \in \mathbb{R}^{H \times W \times C}$ is a weight matrix obtained by amplifying the dimension by point-wise convolution, where each value represents the weighted information post coarse-grained spectral perception. Then multiplying it with the input ensures that each value in the input carries the coarse-grained spectral similarity features brought about by the large receptive field of the large kernel convolution

$$\mathbf{X}_{\text{coarse}} = \mathbf{X}_{\text{weight}} \cdot \mathbf{X}_{\text{fine}}, \quad (11)$$

where $\mathbf{X}_{\text{coarse}} \in \mathbb{R}^{H \times W \times C}$ denotes the results obtained after coarse-grained spectral perception.

4. EXPERIMENTS

4.1. Experimental Settings

Consistent with some previous studies [8, 17, 23, 24], we select 28 bands ranging from 450nm to 650nm for spectral interpolation to obtain data for experimentation. We conduct experiments on both simulated and real HSI datasets.

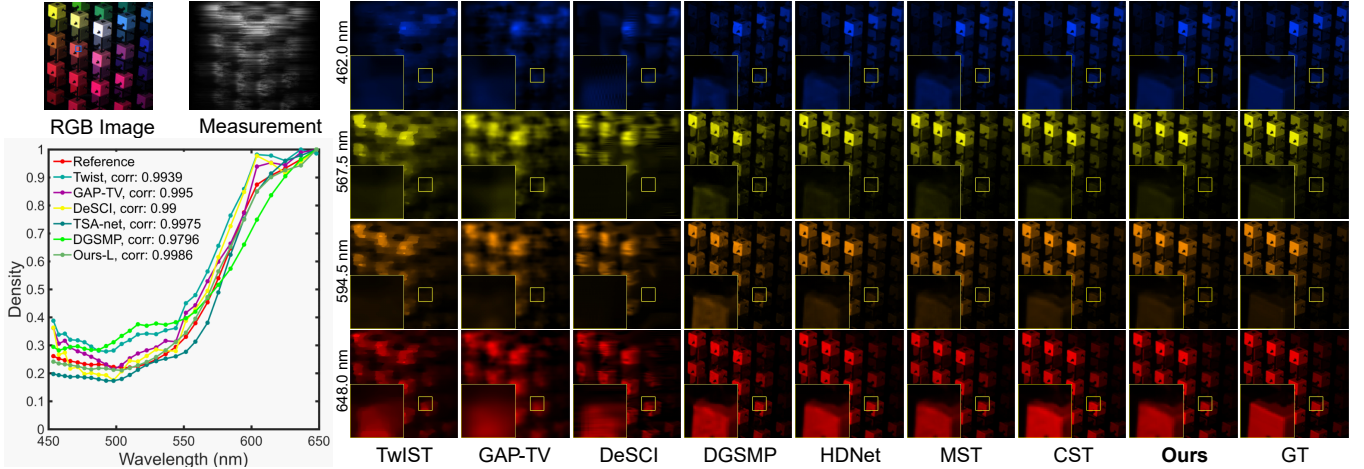


Fig. 4: Comparison of reconstruction results of simulation HSI datasets for 4 out of 28 spectral channels in Scene 2. 7 SOTA methods and our CFSDCN are included here. Zoom in for a better view.

Simulation HSI Data. For the simulation, we engage the CAVE [25] and KAIST [26] datasets, both widely used in the field. The CAVE dataset contains 32 hyperspectral images with dimensions of 256×256 , and the KAIST dataset includes 30 hyperspectral images, each measuring 2704×3376 . Adhering to the methodology established by TSA-Net, we designate CAVE for training and select 10 scenes from KAIST for evaluation purposes.

Real Dataset. Inspired by the approach used in previous works, we conduct tests using a real HSI dataset acquired by the CASSI system to the generalization of our model. We use the real HSI dataset collected by the CASSI system developed in TSA-Net [8].

Evaluation Metrics. The performance of HSI reconstruction is evaluated by Peak Signal-to-Noise Ratio (PSNR) and Structural Similarity Index (SSIM) [27].

Implementation Details. The CFSDCN model, developed using PyTorch, utilizes the Adam optimizer with hyperparameters $\beta_1 = 0.9$ and $\beta_2 = 0.999$. Training spanned 500 epochs, with the learning rate initially set at 4×10^{-4} and reduced by half every 50 epochs. Training samples were generated by randomly cropping 256×256 cubes from a 28-channel HSI cube for simulated data, and 660×660 cubes for actual experimental data. The model employed a dispersion step size of 2 and a batch size of 5, incorporating random rotations and flips for data augmentation. The training and evaluation were performed on a single RTX 3090 GPU.

4.2. Quantitative Results

In our study, we comprehensively compare the CFSDCN method with several current end-to-end methods including model-based methods [4, 28, 20], deep CNN-based methods [22, 12, 8, 21, 6, 13, 9], and Transformer-based methods [17, 23]. To ensure consistency, we re-train all meth-

ods using the same training set and tested them using the same settings as in DGSMP [13]. The PSNR and SSIM results for these methods across ten scenarios in the test set are shown in Tab. 1. The parameters (Params) and floating-point operations (FLOPs) of each method are also given in the table. From these tables, we can observe that our method has significant improvements in reconstruction performance and computational cost.

4.3. Qualitative Results

Simulation HSI Reconstruction. Fig. 4 demonstrates the simulated HSI reconstruction performance of our CFSDCN and other SOTA methods in four spectral channels of Scene 2. We have magnified the images within the yellow box and placed them in the lower-left corner of the picture for a detailed comparison. It can be seen that, compared with over-smoothing, loss of fine-grained structure, or edge distortion and some unwanted color artifacts in other images, our CFSDCN is more effective in reconstructing sharp edge areas, achieving perceptually pleasing image while maintaining uniform spatial smoothness. Furthermore, we plot the spectral density curve of the reconstructed area versus the ground truth (lower left) to demonstrate the effectiveness of our proposed CFSDCN in achieving consistent spectral reconstruction.

Real HSI Reconstruction. We then apply our proposed method to real HSI reconstruction. Following the settings in [13, 17] to ensure fairness, we introduce 11-bit shot noise in the training process to simulate real measurement conditions. As shown in Fig. 5, we compare our method with seven SOTA methods for real scenes. In Scene 1, the reconstruction results obtained from our method demonstrate a smoother appearance, more detailed edge processing, and visually pleasing effects. These outcomes attest to the reliability, robustness, and enhanced generalization capabilities of our approach.

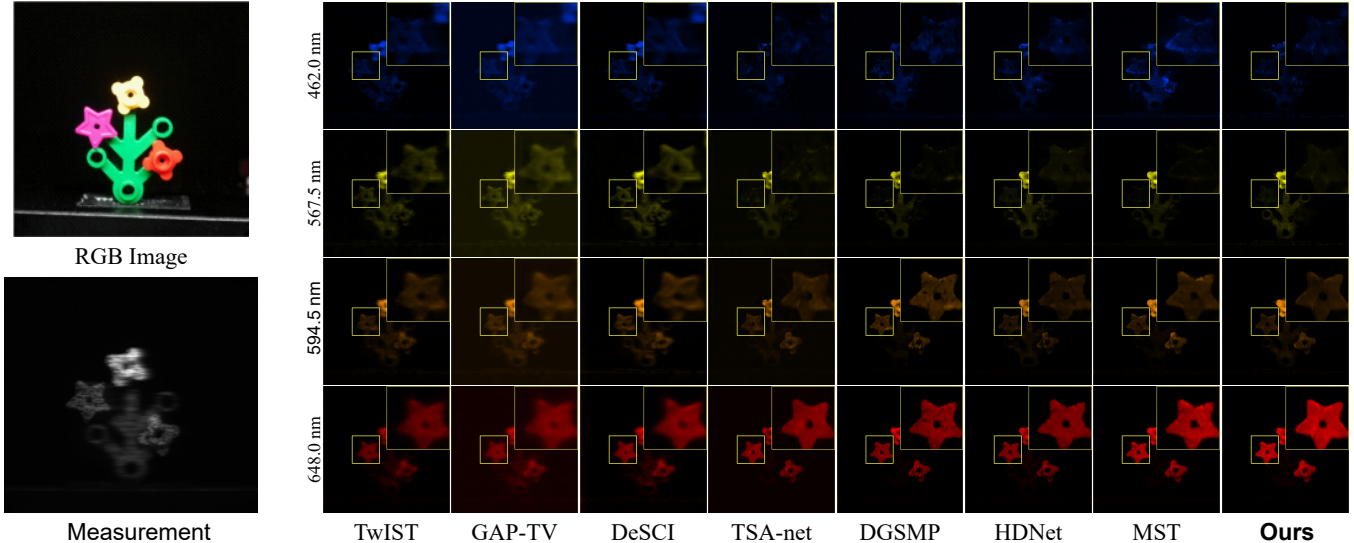


Fig. 5: Comparison of reconstruction results of real HSI datasets for 4 out of 28 spectral channels in Scene 2. 7 SOTA methods and our CFSDCN-M are included here. Zoom in for a better view.

Table 2: Combined Table of Spatial-Spectral-Aware Mechanism, and CNN-based Spectral-Aware Mechanism Comparisons.

(a) Spatial-Spectral-Aware Mechanism Comparison.

Method	Baseline	Conv	G-MSA	W-MSA	Swin-MSA	S-MSA	SAH-MSA	CFSDCN
PSNR	32.57	33.63	35.04	35.02	35.12	35.21	35.53	35.57
SSIM	0.906	0.931	0.944	0.943	0.945	0.946	0.948	0.953
Params(M)	0.51	0.52	1.85	1.85	1.85	1.66	1.36	0.759
FLOPs(G)	6.40	6.69	35.31	24.98	24.98	24.74	24.60	9.45

(b) CNN-based Spectral-Aware Mechanism Comparison.

Method	SEBlock	Conv3×3	Conv7×7	Conv11×11
PSNR	35.37	35.51	35.57	35.56
SSIM	0.951	0.952	0.953	0.952
Params(M)	0.758	0.760	0.764	0.774
FLOPs(G)	9.13	9.37	9.45	9.60

Table 3: Break-down Ablation.

BaseLine	DCB	CFSAB	PSNR	SSIM	Params (M)	FLOPs(G)
✓			33.63	0.931	0.52	6.69
✓	✓		35.28	0.949	0.76	8.71
✓	✓	✓	35.57	0.953	0.76	9.45

4.4. Ablation Study

Break-down Ablation. We conduct a break-down ablation experiment to study the impact of each structure on achieving higher performance. The results are shown in Tab. 3. These results sufficiently demonstrate the effectiveness of both DCB and CFSAB.

Spatial-Spectral-Aware Mechanism Comparison. We compare our CFSDCN with other spatial-spectral-aware mechanisms. These results are showed in Tab. 2 (a). To ensure fairness, we select several models with similar effects for comparison. This result highlights the computational efficiency of our method, mainly because our fully convolutional structure is much more economical than computing self-attention, significantly reducing the computational effort.

CNN-based Spectral-Aware Mechanism Comparison. We primarily compare the effects of SEBlock [29], conv3×3

coarse-grained spectral mechanism, and our LCS (use conv7×7), with results shown in Tab. 2 (b). It is clear that our LCS successfully combines the advantages of these approaches, choosing an appropriately sized convolution kernel to obtain large improvements at a very low overhead.

5. CONCLUSION

In this paper, we present a novel CNN-based method for hyperspectral image (HSI) reconstruction, CFSDCN. Inspired by the inter-spectral characteristics of HSIs and the latest advancements in deformable convolutions, we propose using grouped deformable convolutions to capture spatial features in HSIs. Additionally, we design a convolution-based coarse-fine granularity spectral perception module, which enables the offsets and masks of deformable convolutions to take into account similar information between spectra. Based on this, we have developed a series of highly effective CFSDCN models. Quantitative experiments show that our model significantly outperforms the SOTA algorithm and requires lower computational cost and parameter amount. Qualitative experiments show that our CFSDCN can reconstruct more visually pleasing HSIs.

Acknowledgements This work is partially conducted when Jincheng Yang was a summer intern in Sensing and Computational Imaging (SCI) Lab in 2023. This work was supported by the National Natural Science Foundation of China (grant number 62271414), Zhejiang Provincial Outstanding Youth Science Foundation (grant number LR23F010001) and the Key Project of Westlake Institute for Optoelectronics (grant number 2023GD007).

6. REFERENCES

- [1] M. Fauvel, Y. Tarabalka, J. A. Benediktsson, J. Chanussot, and J. C. Tilton, "Advances in spectral-spatial classification of hyperspectral images," *Proceedings of the IEEE*, 2012.
- [2] M. H. Kim, T. A. Harvey, D. S. Kittle, H. Rushmeier, R. O. P. J. Dorsey, and D. J. Brady, "3d imaging spectroscopy for measuring hyperspectral patterns on solid objects," *ACM Transactions on Graphics*, 2012.
- [3] M. Borengasser, W. S. Hungate, and R. Watkins, *Hyperspectral Remote Sensing: Principles and Applications*, CRC Press, 2007.
- [4] Jose M Bioucas-Dias and Mário A. T. Figueiredo, "A new twist: Two-step iterative shrinkage/thresholding algorithms for image restoration," *IEEE Transactions on Image Processing*, vol. 16, no. 12, pp. 2992–3004, 2007.
- [5] Z. Meng, S. Jalali, and X. Yuan, "Gap-net for snapshot compressive imaging," *arXiv preprint arXiv:2012.08364*, 2020.
- [6] Z. Meng, Z. Yu, K. Xu, and X. Yuan, "Self-supervised neural networks for spectral snapshot compressive imaging," in *ICCV*, 2021.
- [7] Siming Zheng, Yang Liu, Ziyi Meng, Mu Qiao, Zhishen Tong, Xiaoyu Yang, Shensheng Han, and Xin Yuan, "Deep plug-and-play priors for spectral snapshot compressive imaging," *Photonics Research*, vol. 9, no. 2, pp. B18–B29, 2021.
- [8] Ziyi Meng, Jiawei Ma, and Xin Yuan, "End-to-end low cost compressive spectral imaging with spatial-spectral self-attention," in *ECCV*, 2020.
- [9] X. Hu, Y. Cai, J. Lin, H. Wang, X. Yuan, Y. Zhang, R. Timofte, and L. V. Gool, "Hdnet: High-resolution dual-domain learning for spectral compressive imaging," in *CVPR*, 2022.
- [10] Xin Miao, Xin Yuan, Yunchen Pu, and Vassilis Athitsos, " λ -net: Reconstruct hyperspectral images from a snapshot measurement," in *IEEE/CVF Conference on Computer Vision (ICCV)*, 2019.
- [11] Lishun Wang, Zongliang Wu, Yong Zhong, and Xin Yuan, "Snapshot spectral compressive imaging reconstruction using convolution and contextual transformer," *Photonics Research*, vol. 10, no. 8, pp. 1848–1858, 2022.
- [12] L. Wang, C. Sun, M. Zhang, Y. Fu, and H. Huang, "Dnu: Deep non-local unrolling for computational spectral imaging," in *CVPR*, 2020.
- [13] T. Huang, W. Dong, X. Yuan, J. Wu, and G. Shi, "Deep gaussian scale mixture prior for spectral compressive imaging," in *CVPR*, 2021.
- [14] Ziyi Meng, Xin Yuan, and Shirin Jalali, "Deep unfolding for snapshot compressive imaging," *International Journal of Computer Vision*, vol. 131, no. 11, pp. 2933–2958, 2023.
- [15] A. Vaswani, N. Shazeer, N. Parmar, J. Uszkoreit, L. Jones, A. N. Gomez, Ł. Kaiser, and I. Polosukhin, "Attention is all you need," in *NeurIPS*, 2017.
- [16] Ze Liu, Yutong Lin, Yue Cao, Han Hu, Yixuan Wei, Zheng Zhang, Stephen Lin, and Baining Guo, "Swin transformer: Hierarchical vision transformer using shifted windows," in *ICCV*, 2021, pp. 10012–10022.
- [17] Y. Cai, J. Lin, X. Hu, H. Wang, X. Yuan, Y. Zhang, R. Timofte, and L. V. Gool, "Mask-guided spectral-wise transformer for efficient hyperspectral image reconstruction," in *CVPR*, 2022.
- [18] Yubo Dong, Dahua Gao, Tian Qiu, Yuyan Li, Minxi Yang, and Guangming Shi, "Residual degradation learning unfolding framework with mixing priors across spectral and spatial for compressive spectral imaging," in *CVPR*, 2023, pp. 22262–22271.
- [19] Wenhai Wang, Jifeng Dai, Zhe Chen, Zhenhang Huang, Zhiqi Li, Xizhou Zhu, Xiaowei Hu, Tong Lu, Lewei Lu, Hongsheng Li, Xiaogang Wang, and Yu Qiao, "Internimage: Exploring large-scale vision foundation models with deformable convolutions," in *CVPR*, 2023.
- [20] Yang Liu, Xin Yuan, Jinli Suo, David Brady, and Qionghai Dai, "Rank minimization for snapshot compressive imaging," *TPAMI*, 2019.
- [21] X. Miao, X. Yuan, Y. Pu, and V. Athitsos, "L-net: Reconstruct hyperspectral images from a snapshot measurement," in *ICCV*, 2019.
- [22] L. Wang, C. Sun, Y. Fu, M. H. Kim, and H. Huang, "Hyperspectral image reconstruction using a deep spatial-spectral prior," in *CVPR*, 2019.
- [23] Jing Lin, Yuanhao Cai, Xiaowan Hu, Haoqian Wang, Xin Yuan, Yulun Zhang, Radu Timofte, and Luc Van Gool, "Coarse-to-fine sparse transformer for hyperspectral image reconstruction," in *ECCV*, 2022.
- [24] Yuanhao Cai, Jing Lin, Haoqian Wang, Xin Yuan, Henghui Ding, Yulun Zhang, Radu Timofte, and Luc Van Gool, "Degradation-aware unfolding half-shuffle transformer for spectral compressive imaging," in *NeurIPS*, 2022.
- [25] J.I. Park, M.H. Lee, M.D. Grossberg, and S.K. Nayar, "Multispectral imaging using multiplexed illumination," in *ICCV*, 2007.
- [26] I. Choi, M. Kim, D. Gutierrez, D. Jeon, and G. Nam, "High-quality hyperspectral reconstruction using a spectral prior," Tech. Rep., Technical report, 2017.
- [27] Z. Wang, A.C. Bovik, H.R. Sheikh, and E.P. Simoncelli, "Image quality assessment: From error visibility to structural similarity," *IEEE Transactions on Image Processing*, 2004.
- [28] Xin Yuan, "Generalized alternating projection based total variation minimization for compressive sensing," in *ICIP*, 2016.
- [29] Jie Hu, Li Shen, and Gang Sun, "Squeeze-and-excitation networks," in *CVPR*, 2018.